

Phase field simulation of a droplet impacting a solid surface

Qian Zhang,^{a)} Tie-Zheng Qian,^{b)} and Xiao-Ping Wang^{c)}

Department of Mathematics, The Hong Kong University of Science and Technology, Clear Water Bay, Kowloon, Hong Kong, China

(Received 5 April 2015; accepted 14 January 2016; published online 8 February 2016)

We simulate a droplet impacting on a solid surface using a phase field model consisting of the Cahn-Hilliard and Navier Stokes equations with the generalized Navier boundary condition. An efficient gradient stable scheme is used to solve the system in axisymmetric coordinates. Our objective is to understand numerically the mechanisms leading to different impacting phenomena such as adherence, bouncing, partial bouncing, and splashing. In particular, we study how various processes are affected by the relevant dimensionless parameters: the Reynolds number, Weber number, density ratio, viscosity ratio, and the wettability of the solid surface. We also compare our numerical results with the experimental results and observe almost quantitative agreement. © 2016 AIP Publishing LLC. [<http://dx.doi.org/10.1063/1.4940995>]

I. INTRODUCTION

The dynamics of a droplet impacting on solid surfaces has been the subject of intense study for more than a century and is of great interest in many industrial and environmental processes. Examples include rain falling in nature, treating leaves with pesticides in agriculture, and waterproofing fabrics in materials science. The outcome of droplet impact depends on the impact velocity, droplet size, properties of the liquid (its density, viscosity), interfacial tension, and roughness and wettability of the solid surface. In general, three different types of behaviors are observed in the process of droplet impact: adherence, bouncing, and splashing. Adherence is commonly observed with water drops on wetting surfaces, as well as with any viscous fluid, for which a large viscosity would result in a relatively large energy dissipation. Bouncing occurs most readily on hydrophobic surfaces, when the velocity of the droplet upon impact is not too high. Splashing is observed when the kinetic energy overcomes the cohesion of the surface tension, and the droplet breaks into many smaller droplets.²¹

For small droplets, gravity can be neglected and a droplet impacting on a flat, smooth, and chemically homogeneous solid surface is then controlled by three dimensionless parameters, the Reynolds number $Re = \rho_L V D_0 / \eta_L$, and the Weber number $We = \rho_L V^2 D_0 / \gamma$, and the static contact angle of the surface θ_s , where D_0 is the diameter of the droplet; V is the impact velocity; γ is the interfacial surface tension between the impacting liquid and the ambient fluid; ρ_L , η_L are the liquid density and liquid viscosity, respectively. Physically, the Reynolds number Re measures the inertial force relative to the viscous force; the Weber number We measures the kinetic energy relative to the surface energy; and the equilibrium contact angle θ_s measures the wettability of the solid surface. Their effects on the outcome of droplet impact are the focus of our numerical study in this paper.

Large amounts of experimental work have been conducted on droplet impact.^{3,8,9,18,22–24,27} A review of previous work in this field is provided by Yarin.² Most of these experiments focus on the effects of droplet size, impact velocity, viscosity, surface tension as well as surface roughness, and wettability. The influence of various parameters on droplet spreading upon impact is quantitatively

^{a)}Electronic mail: qzhangxd@ust.hk. Current address: Department of Engineering Sciences and Applied Mathematics, Northwestern University, 2145 Sheridan Road, Evanston, Illinois 60208-3125, USA.

^{b)}Electronic mail: maqian@ust.hk

^{c)}Author to whom correspondence should be addressed. Electronic mail: mawang@ust.hk

determined by Rioboo *et al.*²⁴ Details of the kinematics of the moving contact line during the spreading process are revealed by Šikalo *et al.*²⁷ It has been shown experimentally that a water droplet can fully bounce, like a solid particle, when impinging on a super-hydrophobic surface.⁹ For a range of Weber and Reynolds numbers, surface roughness plays an important role.⁴ It has also been shown by Xu *et al.*¹⁸ that the surrounding gas can have a strong influence on splashing.

Numerical simulation serves as a good complement to the experimental and theoretical studies. A number of numerical studies have been reported using the level set method,^{5,9,13,14} volume of fluid,^{17,25} and lattice Boltzmann method.^{28,35} A diffuse interface model coupled with hydrodynamics and with no slip boundary condition on the solid boundary is adopted by Khatavkar *et al.* to simulate the dynamics of droplet impact.³²

An accurate description of the dynamics of the contact line is important in modeling the impact dynamics. A phase field model consisting of a coupled system of the Cahn-Hilliard (CH) equation and Navier-Stokes (NS) equations with the generalized Navier boundary condition (GNBC) is proposed by Qian, Wang, and Sheng^{29–31} to model the moving contact line problem. The numerical results based on the GNBC can reproduce quantitatively the results from MD simulation²⁹ and from experiments.²⁶ The model has also been used to study two-phase flows on patterned surfaces.³³ Our new model has the advantage of providing a more accurate description of contact line motion which is an important factor in droplet impacting and spreading on solid surfaces. Using the phase field model also enables us to handle the topological changes of the droplet shape more easily. In this paper, this phase field model in axisymmetric coordinates is used to numerically investigate the dynamics of droplet impact on solid surfaces. The numerical method is based on the energy stable scheme developed by Gao and Wang.^{19,20} Our objective is to quantify the influence of individual parameters on the droplet impact dynamics. Ranges of the Weber number, Reynolds number, and equilibrium contact angle leading to phenomena of adherence, bouncing, partial bouncing, and splashing are obtained. The effect of slip length, density ratio, and viscosity ratio is also studied. Droplet-impact maps are generated under axisymmetric conditions, in which the outcomes of the impact are characterized by different effects of these parameters.

Using the model in axisymmetric coordinates enables us to reduce the computational cost significantly. However, this also implies that we cannot simulate the real splashing when the impacting droplet breaks into smaller bouncing droplets which is essentially a nonsymmetric phenomenon. In the axisymmetric case, we define splashing (see Section III C) to be the case when the impacting droplet breaks into multiple rings that bounce off (which would break into small droplets in a fully three-dimensional simulation).

The rest of this paper is organized as follows. In Section II, we introduce the model and numerical schemes used to simulate a droplet impacting on solid surfaces. Numerical results of droplet impact are presented and discussed in Section III. The paper concludes in Section IV.

II. MATHEMATICAL MODEL

We consider a spherical droplet of one fluid (liquid L) with diameter D_0 , density ρ_L , and viscosity η_L surrounded by another fluid (air V) with density ρ_V and viscosity η_V . The droplet impacts vertically on a solid surface S with velocity V_0 . The interfacial tension of liquid L and air V is given by γ (denoted by γ_{LV} in Figure 1). Surface tensions between liquid L and solid surface S and between air V and solid surface S are given by γ_{SL} and γ_{SV} , respectively. Slip coefficients between liquid L and the solid surface and between air V and the solid surface are β_L and β_V , respectively. A schematic diagram is shown in Figure 1.

A. Governing equations

In the non-splashing case, we can assume that the system is axisymmetric. Therefore, in the cylindrical domain,

$$\Omega = \{(r, z, \theta) \mid 0 \leq r \leq R, 0 \leq z \leq L, 0 \leq \theta \leq 2\pi\}.$$

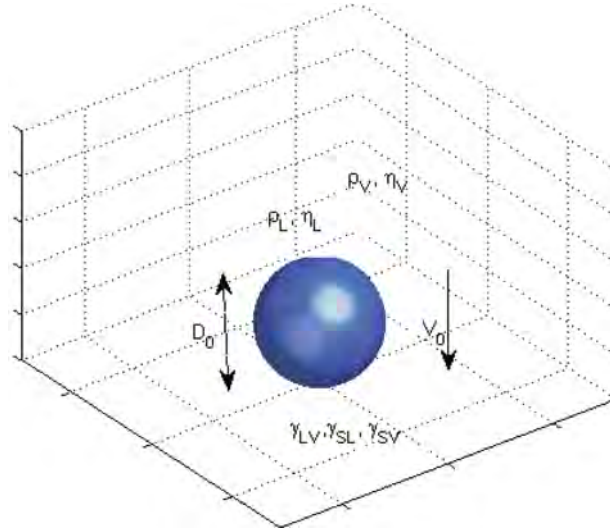


FIG. 1. Schematic diagram of a droplet impacting on a solid surface.

We consider the coupled CH and NS system,

$$\frac{\partial \phi}{\partial t} + \mathbf{v} \cdot \nabla \phi = M \Delta \mu, \quad \mu = -K \Delta \phi - r \phi + u \phi^3, \quad \text{in } \Omega, \quad (1)$$

$$\rho \left[\frac{\partial \mathbf{v}}{\partial t} + (\mathbf{v} \cdot \nabla) \mathbf{v} \right] = -\nabla p + \nabla \cdot [\eta D(\mathbf{v})] + \mu \nabla \phi, \quad \text{in } \Omega, \quad (2)$$

$$\nabla \cdot \mathbf{v} = 0. \quad \text{in } \Omega. \quad (3)$$

Density and viscosity are obtained as interpolations between ρ_L and ρ_V and between η_L and η_V using ϕ , i.e.,

$$\rho = \rho_L \frac{1 - \phi}{2} + \rho_V \frac{1 + \phi}{2}, \quad \eta = \eta_L \frac{1 - \phi}{2} + \eta_V \frac{1 + \phi}{2}. \quad (4)$$

Here, $\mathbf{v} = (v_r, v_z)$, where v_r, v_z denote velocities along the r, z directions, respectively. p is the pressure. η is the dynamic viscosity. ρ is the mass density. M is the phenomenological mobility coefficient. $\mu \nabla \phi$ is the capillary force. $K, r,$ and u are parameters related to the interface thickness $\zeta = \sqrt{K}/r$, interfacial tension $\gamma = 2\sqrt{2}r^2\zeta/3u$, and two homogeneous equilibrium phases $\phi_{\pm} = \pm\sqrt{r}/u$ ($= \pm 1$ in our problem). In the axisymmetric cylindrical coordinate system, we have

$$\Delta = \frac{1}{r} \partial_r + \partial_r^2 + \partial_z^2, \quad \nabla = (\partial_r, \partial_z), \quad \nabla \cdot \mathbf{v} = \frac{1}{r} \frac{\partial(rv_r)}{\partial r} + \frac{\partial v_z}{\partial z},$$

$$\nabla \cdot [\eta D(\mathbf{v})] = \nabla \cdot [\eta(\nabla \mathbf{v} + \nabla \mathbf{v}^T)] = \left(\begin{array}{l} \frac{2}{r} \frac{\partial}{\partial r} (r\eta \frac{\partial v_r}{\partial r}) - \frac{\eta}{r^2} v_r + \frac{\partial}{\partial z} (\eta \frac{\partial v_r}{\partial z}) + \frac{\partial}{\partial z} (\eta \frac{\partial v_z}{\partial r}) \\ \frac{1}{r} \frac{\partial}{\partial r} (r\eta \frac{\partial v_r}{\partial z}) + \frac{1}{r} \frac{\partial}{\partial r} (r\eta \frac{\partial v_z}{\partial r}) + 2 \frac{\partial}{\partial z} (\eta \frac{\partial v_z}{\partial z}) \end{array} \right).$$

B. Boundary conditions

To describe the motion of the contact line on the solid boundary $z = 0$, Eqs. (2) and (3) are supplemented with the GNBC,³¹

$$\beta(\phi) v_r^{slip} = -\eta \partial_n v_r + L(\phi) \partial_r \phi. \quad (5)$$

Here, $L(\phi) = K \partial_n \phi + \partial \gamma_{wf}(\phi) / \partial \phi$ and $\gamma_{wf}(\phi) = -\gamma \cos \theta_s \sin(\pi\phi/2)/2$ where θ_s is the equilibrium contact angle and $\cos \theta_s = (\gamma_{SV} - \gamma_{SL})/\gamma$. $\beta(\phi) = (1 - \phi)\beta_L/2 + (1 + \phi)\beta_V/2$ is an interpolation between the slip coefficients of the two fluids. $v_r^{slip} = v_r$ is the slip velocity on the solid surface.

In addition, a relaxation boundary condition is imposed on the phase field variable ϕ at the solid surface $z = 0$

$$\frac{\partial \phi}{\partial t} + v_r \partial_r \phi = -\Gamma[L(\phi)], \quad (6)$$

where Γ is a (positive) phenomenological parameter, together with the impermeability conditions

$$v_z = 0, \quad \partial_z \mu = 0, \quad (7)$$

and natural boundary conditions on the other boundaries of the computational domain,

$$v_r = 0, \quad \partial_r v_z = 0, \quad \partial_r \phi = 0, \quad \partial_r \mu = 0, \quad \text{on } r = 0, \quad (8)$$

$$\partial_r v_r = 0, \quad \partial_r v_z = 0, \quad \partial_r \phi = 0, \quad \partial_r \mu = 0, \quad \text{on } r = R, \quad (9)$$

$$\partial_z v_r = 0, \quad v_z = 0, \quad \partial_z \phi = 0, \quad \partial_z \mu = 0, \quad \text{on } z = L. \quad (10)$$

C. Dimensionless equations

To obtain the dimensionless equations, we scale length by D_0 , ϕ by $\sqrt{r/u}$ ($=1$, in this paper), velocity by V_0 , time by D_0/V_0 , density by liquid density ρ_L , viscosity by liquid viscosity η_L , and pressure by $\eta_L V_0/D_0$. We use the same symbols to represent the dimensionless variables in the following. Then, in the dimensionless domain,

$$\Omega = \{(r, z, \theta) \mid 0 \leq r \leq R/D_0, 0 \leq z \leq L/D_0, 0 \leq \theta \leq 2\pi\},$$

and the dimensionless form of Eqs. (1)-(7) is as follows:

$$\frac{\partial \phi}{\partial t} + \mathbf{v} \cdot \nabla \phi = \mathcal{L}_d \Delta \mu, \quad \mu = -\epsilon \Delta \phi - \phi/\epsilon + \phi^3/\epsilon, \quad \text{in } \Omega, \quad (11)$$

$$\mathcal{R}e \rho \left[\frac{\partial \mathbf{v}}{\partial t} + (\mathbf{v} \cdot \nabla) \mathbf{v} \right] = -\nabla p + \nabla \cdot [\eta D(\mathbf{v})] + \mathcal{B} \mu \nabla \phi, \quad \text{in } \Omega, \quad (12)$$

$$\nabla \cdot \mathbf{v} = 0, \quad \text{in } \Omega. \quad (13)$$

Here, ϵ is the ratio between interface thickness ζ and characteristic length D_0 ; density is $\rho = (1 - \phi)/2 + \lambda_\rho(1 + \phi)/2$; viscosity is $\eta = (1 - \phi)/2 + \lambda_\eta(1 + \phi)/2$, where $\lambda_\rho = \rho_V/\rho_L$ and $\lambda_\eta = \eta_V/\eta_L$ are the density ratio and viscosity ratio, respectively.

The boundary conditions along the solid surface $z = 0$ are

$$\frac{\partial \phi}{\partial t} + v_r \partial_r \phi = -\mathcal{V}_s [L(\phi)], \quad (14)$$

$$v_z = 0, \quad \partial_z \mu = 0, \quad (15)$$

$$[\mathcal{L}_s l_s]^{-1} v_r^{slip} = \mathcal{B} L(\phi) \partial_r \phi / \eta - \partial_z v_r. \quad (16)$$

Here, $L(\phi) = \epsilon \partial_z \phi + \partial \gamma_{wf}(\phi)/\partial \phi$ and $\gamma_{wf}(\phi) = -\sqrt{2} \cos \theta_s \sin(\pi\phi/2)/3$. Slip length $l_s = (1 - \phi)/2 + \lambda_{l_s}(1 + \phi)/2$ is an interpolation between two different wall-fluid slip lengths where $\lambda_{l_s} = l_{SV}/l_{SL}$. Here, $l_{SV} = \eta_V/\beta_V$ and $l_{SL} = \eta_L/\beta_L$. Dimensionless forms of the boundary conditions Eqs. (8)-(10) are the same as their dimensional forms,

$$v_r = 0, \quad \partial_r v_z = 0, \quad \partial_r \phi = 0, \quad \partial_r \mu = 0, \quad \text{on } r = 0, \quad (17)$$

$$\partial_r v_r = 0, \quad \partial_r v_z = 0, \quad \partial_r \phi = 0, \quad \partial_r \mu = 0, \quad \text{on } r = R/D_0, \quad (18)$$

$$\partial_z v_r = 0, \quad v_z = 0, \quad \partial_z \phi = 0, \quad \partial_z \mu = 0, \quad \text{on } z = L/D_0. \quad (19)$$

Eight dimensionless parameters appear in the above equations. They are: (1) $\mathcal{L}_d = 3M\gamma/2\sqrt{2}V_0D_0^2$; (2) $\mathcal{R}e = \rho_L V_0 D_0 / \eta_L$, which measures the relative importance of inertial force to viscous force; (3) $\mathcal{B} = 3\gamma/2\sqrt{2}\eta_L V_0 (= 3\mathcal{R}e/2\sqrt{2}\mathcal{W}e)$, which is inversely proportional to the capillary number $Ca = \eta_L V_0 / \gamma$ which measures the relative importance of the viscous force to surface tension; (4) $\mathcal{V}_s = 3\gamma\Gamma D_0 / 2\sqrt{2}V_0$; (5) $\mathcal{L}_s = \eta_L / \beta_L D_0$, which is the slip length of the liquid scaled by D_0 ; (6) $\lambda_{l_s}, \lambda_\rho, \lambda_\eta$ are the slip length, the density ratio, and viscosity ratio between the ambient fluid and the liquid, respectively.

Moreover, according to the physical problem we are investigating, the initial conditions are given by

$$\phi(r, z, t = 0) = \tanh\left(\frac{\sqrt{r^2 + (z - \frac{1}{2})^2} - \frac{1}{2}}{\sqrt{2}\epsilon}\right), \quad (20)$$

$$v_z(r, z, t = 0) = -\frac{1}{2}\left(1 - \tanh\left(\frac{\sqrt{r^2 + (z - \frac{1}{2})^2} - \frac{1}{2}}{\sqrt{2}\epsilon}\right)\right), \quad v_r(r, z, t = 0) = 0. \quad (21)$$

Remark 2.1. Here, we assume that initially the droplet surface ($\phi = 0$) comes into contact with the solid surface at $(r, z) = (0, 0)$. We also assume that the density ratio is large enough ($\frac{\rho_L}{\rho_V} \geq 100$) such that the initial velocity of the ambient fluid can be neglected.

D. Energy law of the model

There are three components to the total free energy (F_t) in the system we are considering, i.e., the kinetic energy (F_k), the bulk free energy (F_b) and the surface energy at the fluid-solid surface (F_{wf}). According to Qian *et al.*,³⁰ dissipative mechanisms introduced in the model consist of the dissipation due to viscosity (R_v), the dissipation due to slipping (R_s), the dissipation due to diffusion in the bulk (R_d) and the dissipation due to relaxation at the solid surfaces (R_r). In summary, the energy law of the model is

$$\frac{d}{dt}(F_k + F_{wf} + F_b) = -(R_v + R_s + R_d + R_r), \quad (22)$$

where

$$R_v = \frac{1}{2} \|\sqrt{\eta} D(\mathbf{v})\|^2 \triangleq \mathcal{R}_v, \quad R_s = \mathcal{L}_s^{-1} \|(\eta/l_s)^{1/2} v_r^{slip}\|_{z=0}^2 \triangleq \mathcal{L}_s^{-1} \mathcal{R}_s,$$

$$R_d = \mathcal{B} \mathcal{L}_d \|\nabla \mu\|^2 \triangleq \mathcal{B} \mathcal{L}_d \mathcal{R}_d, \quad R_r = \mathcal{B} \mathcal{V}_s \|L(\phi)\|_{z=0}^2 \triangleq \mathcal{B} \mathcal{V}_s \mathcal{R}_r,$$

and

$$F_k = \mathcal{R}e \frac{1}{2} \|\sqrt{\rho} \mathbf{v}\|^2 \triangleq \mathcal{R}e \mathcal{F}_k, \quad F_{wf} = \mathcal{B} \int_{z=0} \gamma_{wf}(\phi) ds \triangleq \mathcal{B} \mathcal{F}_{wf},$$

$$F_b = \mathcal{B} \int_{\Omega} \left[\frac{1}{2} \epsilon |\nabla \phi|^2 + \frac{(\phi^2 - 1)^2}{4\epsilon} \right] dx \triangleq \mathcal{B} \mathcal{F}_b.$$

Here, ϕ, \mathbf{v} are the smooth solutions to the system Eqs. (11)-(19) and $\|\cdot\|$ represents the L_2 norm on domain Ω , or on the solid boundary $z = 0$. Moreover, energy law Eq. (22) is equivalent to

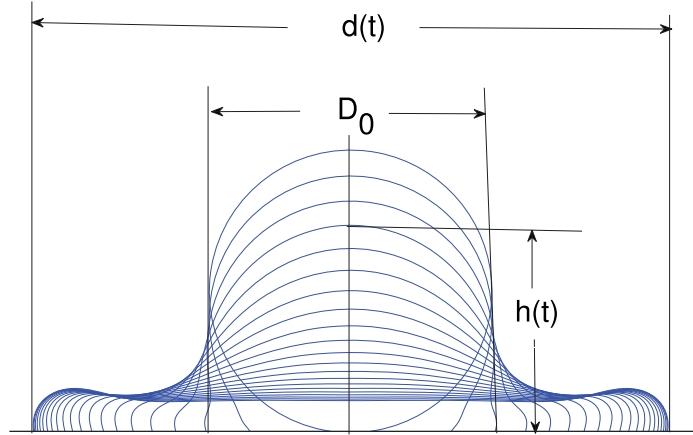
$$\frac{d}{dt} \left[\frac{2\sqrt{2}}{3} \mathcal{W}e \mathcal{F}_k + \mathcal{F}_{wf} + \mathcal{F}_b \right] = - \left(\frac{2\sqrt{2}}{3} \frac{\mathcal{W}e}{\mathcal{R}e} \mathcal{R}_v + \frac{2\sqrt{2}}{3} \frac{\mathcal{W}e}{\mathcal{R}e} \mathcal{L}_s^{-1} \mathcal{R}_s + \mathcal{L}_d \mathcal{R}_d + \mathcal{V}_s \mathcal{R}_r \right). \quad (23)$$

III. NUMERICAL RESULTS

The CH and NS equations (11)-(19) are solved using the numerical scheme proposed by Gao and Wang²⁰ (see Subsection 1 of the Appendix). The Staggered mesh is used to improve the stability of the numerical scheme and to avoid the singularity on the central line $r = 0$ introduced by the cylindrical coordinate system (see Subsection 2 of the Appendix).

We study the effects of dimensionless parameters on the outcome of a droplet impacting on solid surfaces. Usually, four possible phenomena are observed, adherence, partial bouncing, bouncing, and splashing. The dynamic process of a droplet impacting on solid surfaces can be described by the droplet spreading diameter and the droplet height,

$$\xi(t) = \frac{d(t)}{D_0}, \quad H(t) = \frac{h(t)}{D_0}.$$

FIG. 2. Definitions of $d(t)$, $h(t)$ and D_0 .

Here, $d(t)$ represents the diameter of the contact area between the droplet and the solid surface and $h(t)$ is the height of the droplet at the center ($r = 0$) at time t (see Fig. 2). The maximum spreading diameter d_m is defined as $d_m = \max_{t>0} \xi(t)$. The time it takes to reach d_m is denoted by t_m . Parameters that may influence the outcome of the impact are the Reynolds number $\mathcal{R}e$, Weber number $\mathcal{W}e$, equilibrium contact angle θ_s , density ratio λ_ρ , and viscosity ratio λ_η of the droplet L and the surrounding fluid V . Other parameters in the numerical simulations are taken as follows:

$$\begin{aligned} \rho_V &= 1.29 \text{ kg/m}^3 \quad (\text{density of air}), & \rho_L &= 0.998 \times 10^3 \text{ kg/m}^3 \quad (\text{density of water}), \\ \eta_V &= 1.79 \times 10^{-5} \text{ kg/(m s)} \quad (\text{viscosity of air}), \\ \eta_L &= 1.002 \times 10^{-3} \text{ kg/(m s)} \quad (\text{viscosity of water}), \\ \mathcal{L}_d &= 1.0 \times 10^{-4}, \quad \mathcal{V}_s = 500, \quad \mathcal{L}_s = 0.0025, \quad \lambda_{t_s} = 1, \quad \epsilon = 0.01. \end{aligned} \quad (24)$$

Remark 3.1. The phenomenological parameters \mathcal{L}_d and \mathcal{V}_s are chosen under the suggestion of Carlson *et al.*¹ based on the data from the kinetic molecular theory. We point out that \mathcal{L}_d and \mathcal{V}_s may vary from liquid to air. Studies have shown that composition-dependent mobility does have an effect on the coarsening kinetics of a two-phase system (see, e.g., work by Zhu *et al.*¹⁵). However, in the dynamic processes considered in this paper, the effects of diffusion and boundary relaxation are weak. Therefore, we simply use constants for simplicity.

We now investigate the influence of liquid properties and impact velocity on the outcome of the impact using the two dimensionless parameters, the Reynolds number $\mathcal{R}e$ and the Weber number $\mathcal{W}e$. The property of the solid surface is simply characterized by the equilibrium contact angle θ_s . Other parameters in the numerical simulations are taken as in (24).

A. Effect of Reynolds number

We first fix the Weber number $\mathcal{W}e = 150$ and the static contact angle $\theta_s = 90^\circ$ and study the droplet impact behavior for different values of the Reynolds number $\mathcal{R}e = 10, 50, 100, 500, 1000$. In each case, the droplet spreading diameter as a function of time $\xi(t)$ is shown in Fig. 3(a). The maximum spreading diameter d_m increases as $\mathcal{R}e$ increases. The time it takes to reach the maximum t_m remains unchanged. The behavior in the spreading stage (before the maximum d_m is reached) is similar for different Reynolds numbers. However, the behavior in the recoil stage varies as the Reynolds number increases. For relatively small Reynolds numbers ($\mathcal{R}e = 10, 50, 100$), $\xi(t)$ decreases monotonically to a constant indicating droplet adherence. Fig. 4 shows the evolution of droplet shapes when $\mathcal{R}e = 100$. As the Reynolds number is increased, the outcome of the impact ranges from partial bouncing at $\mathcal{R}e = 500$ (in which the droplet stays partially on the surface and launches one or more smaller drops at its top in the process of receding) to complete bouncing at $\mathcal{R}e = 1000$.

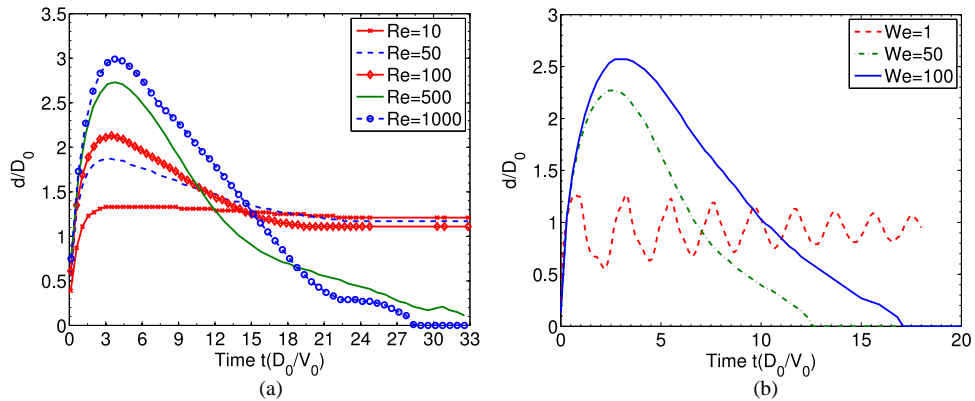


FIG. 3. (a) Time evolution of dimensionless spreading diameter $\xi(t)$ for different Reynolds numbers ($Re = 10, 50, 100, 500, 1000$) with fixed $\theta_s = 90^\circ$ and $We = 150$. (b) Time evolution of $\xi(t)$ for different Weber numbers ($We = 1, 50, 100$) with fixed $\theta_s = 110^\circ$ and $Re = 800$.

Fig. 5 shows the impacting process for $Re = 1000$. In the spreading stage, the maximum diameter is reached at around $t = 4$ (Fig. 5(c)) when a rim is formed on the periphery of the droplet followed by a thin film. In the recoil stage, capillary wave instability results in rapturing of the thin film, creating a ring structure with dried out regions. The droplet then recoils aggressively and lifts off entirely from the solid surface at approximately $t = 19$. The emergence of a ring structure with a dry-out region for large enough Re and We was also recently reported experimentally and numerically by Renardy *et al.*³⁴

Note that here a large We has been used. This means that the initial kinetic energy is much larger than the initial surface energy of the (spherical) droplet. As the viscous dissipation is weak, after the

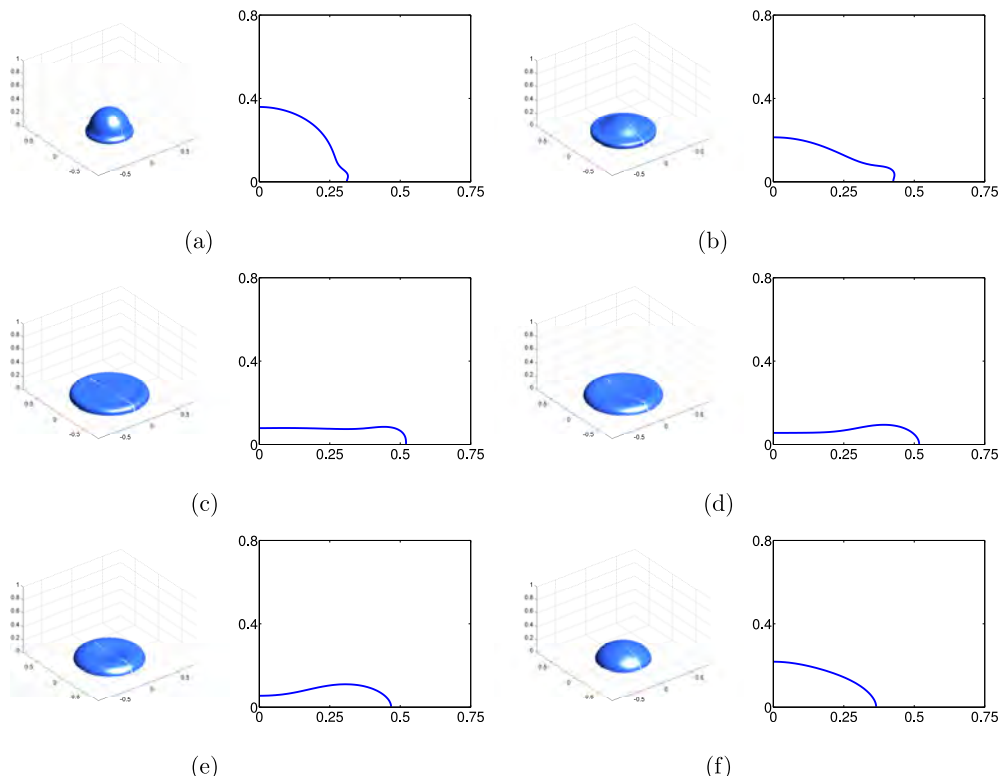


FIG. 4. Droplet shapes with the corresponding profiles in the radial direction at different times for $Re = 100$ and $We = 150$, $\theta_s = 90^\circ$. Adherence is observed in this case. (a) $t = 0.32$, (b) $t = 0.72$, (c) $t = 1.6$, (d) $t = 3.2$, (e) $t = 4.8$, and (f) $t = 8.0$.

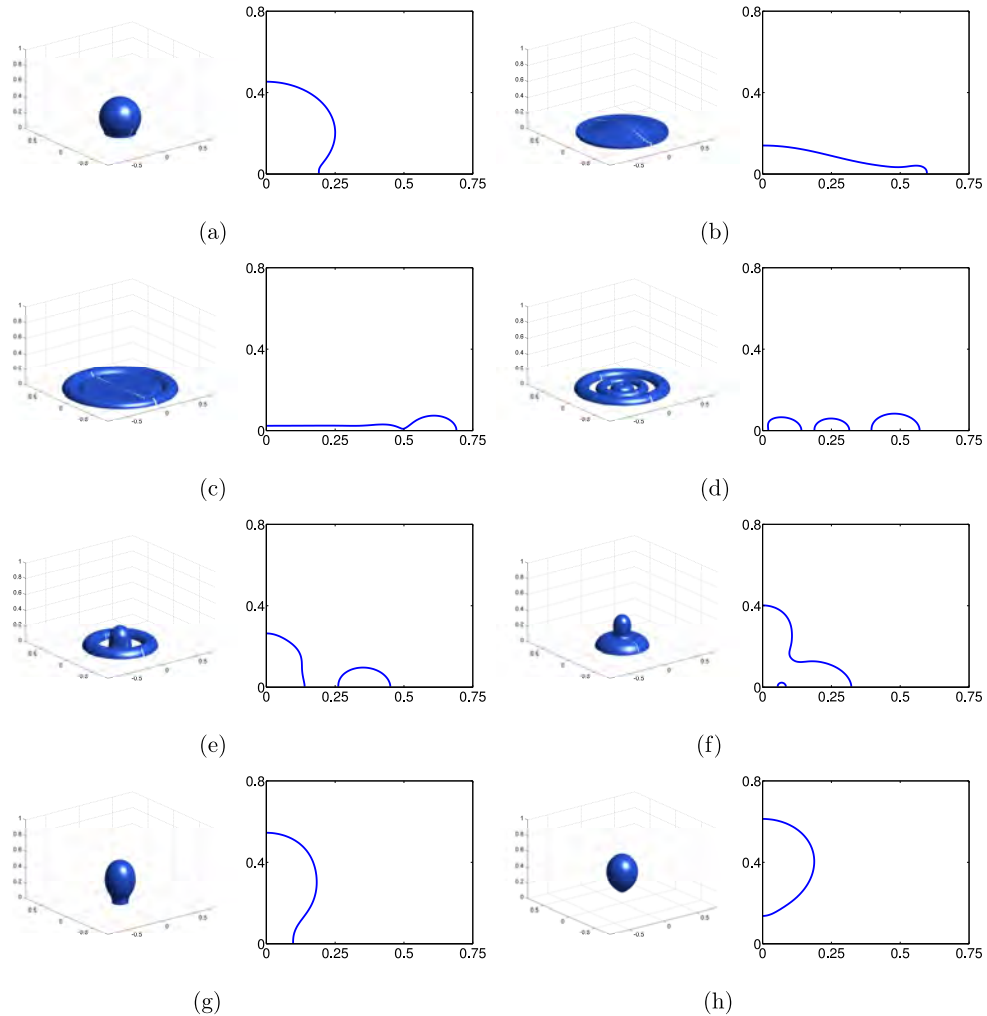


FIG. 5. Droplet shapes with the corresponding profiles in the radial direction at different times for $Re = 1000$ and $We = 150$, $\theta_s = 90^\circ$. Complete bouncing is observed in this case. (a) $t = 0.1$, (b) $t = 1.0$, (c) $t = 4.0$, (d) $t = 6.0$, (e) $t = 8.0$, (f) $t = 10.0$, (g) $t = 14.0$, and (h) $t = 19$.

impact, there should be enough kinetic energy transformed into surface energy via droplet spreading. Much of the surface energy will subsequently be transformed into kinetic energy for upward movement. This results in partial or complete bouncing. The weak viscous dissipation necessitated by bouncing simply means a large Re , as observed in our simulations. At small Re , viscous dissipation consumes a significant portion of the initial kinetic energy. As a result, the maximum spreading diameter is reduced and no bouncing will occur, i.e., droplet adherence is expected. Furthermore, at large Re , the droplet spreading is dominated by a balance between the inertial force and the capillary force.^{10,11} As a result, the time needed to reach the maximum diameter t_m scales as $\sqrt{We}D_0/V_0$, in agreement with the observation that it is nearly independent of Re .

Remark 3.2. Notice that $\mathcal{B} = 3Re/2\sqrt{2}We$. As we vary Re with We fixed, we also need to vary \mathcal{B} accordingly in the model. This is also the case when we vary We with Re fixed.

B. Effect of Weber number

We now fix the Reynolds number at $Re = 800$ and the static contact angle at $\theta_s = 110^\circ$ and study the droplet impacting behavior for different values of the Weber number $We = 1, 50, 100$. In each case, the droplet spreading diameter as a function of time $\xi(t)$ is shown in Fig. 3(b). The maximum

spreading diameter increases as the Weber number increases. It also takes longer to reach the first maximum diameter for a larger Weber number. However, the behavior in the recoil stage is quite different as the Weber number increases. For a relatively small Weber number ($We = 1$), the balance between kinetic energy and surface tension causes the droplet to oscillate between advancing and receding before reaching a steady state. For Weber numbers $We = 50, 100$, we observe complete bouncing.

Note that here a large Reynolds number Re has been used. This means that viscous dissipation is weak. Therefore, the observed phenomena are governed by a competition between the inertial force and the capillary force. At large We , as explained above, bouncing is expected. At small We , however, the initial kinetic energy is not that large compared to the initial surface energy of the (spherical) droplet. Consequently, droplet deformation is limited as seen in the case of $We = 1$. The balance between the inertial force and the capillary force (which is an elastic force) then results in an oscillatory motion with the amplitude decreasing in time, i.e., the droplet behaves like an underdamped oscillator.

C. Effect of wettability

Given Weber number $We = 120$ and Reynolds number $Re = 800$, we study the effect of wettability (θ_s) of the solid surface. Fig. 6(a) shows that the maximum spreading diameter d_m decreases as θ_s increases. However, the time it takes to reach the maximum spreading diameter d_m remains the same. The total contact time of the droplet with the surface also decreases as θ_s increases. Physically, as θ_s increases, the solid surface will more energetically repel the liquid droplet. This leads to a reduction in the maximum spreading diameter and a reduction in the contact time as well. In Figure 6(b), we also plot the droplet height $H(t)$ (at the center) as a function of time. The droplet quickly reaches the minimum height even before the maximum spreading diameter is reached. The droplet height then increases continuously as the droplet recoils.

As superhydrophobicity hinders the droplet spreading and suppresses the resultant viscous dissipation, it is much easier for the droplet to bounce and splash on a superhydrophobic surface as shown in Fig. 7(a) for $\theta_s = 160^\circ$ where complete bouncing is observed at $Re = 50$ and splashing is expected at $Re = 1000$. The effect of wettability can be revealed by comparing Fig. Fig. 3(a) ($\theta_s = 90^\circ$ and $We = 150$) and Fig. 7(a) ($\theta_s = 160^\circ$ and $We = 150$), which shows that superhydrophobicity allows bouncing to occur at a lower Re (or a higher viscosity), as the viscous dissipation is better suppressed on more hydrophobic surfaces. The effect of wettability is also summarized in the impact map in Fig. 8(a).

Fig. 9 shows the process of spreading and partial bouncing for the case with $Re = 1000$, $We = 150$, and $\theta_s = 160^\circ$. After the impact, the droplet quickly spreads and a rim is formed at the front edge of the droplet as it reaches the maximum spreading diameter. The surface tension then causes part of the droplet to recoil. Multiple rim structures emerge and the outer rim on the periphery overcomes the

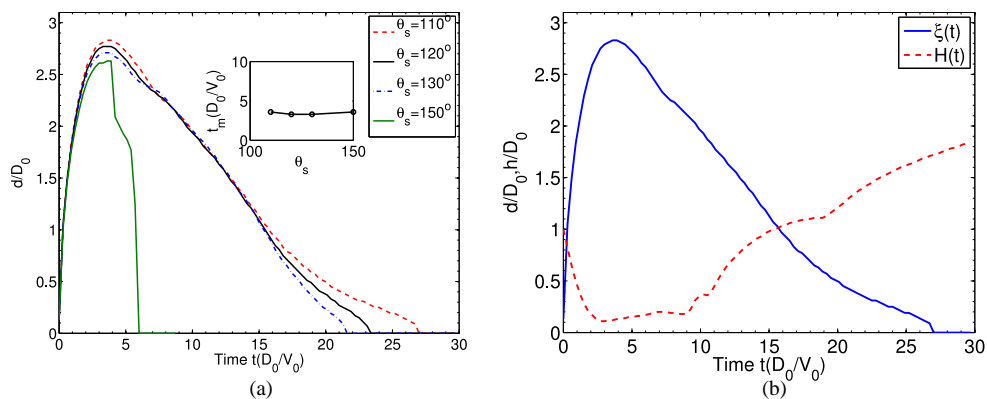


FIG. 6. (a) Time evolution of $\xi(t)$ for different equilibrium contact angles. The inset shows the time needed to reach the maximum spreading diameters (t_m) for different θ_s . (b) Time evolution of $\xi(t)$ and $H(t)$ for $\theta_s = 110^\circ$ with $We = 200$, $Re = 800$.

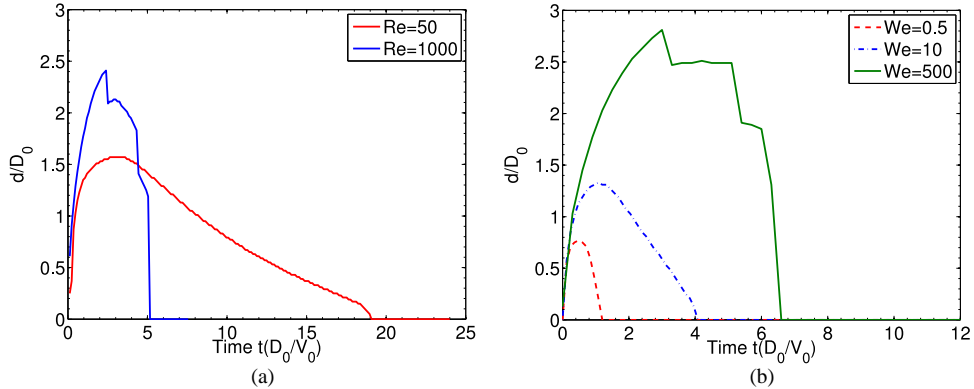


FIG. 7. (a) Time evolution of dimensionless spreading diameter ($\xi(t)$) for Reynolds numbers $Re = 50, 1000$ with $\theta_s = 160^\circ$ and $We = 150$. (b) Time evolution of dimensionless spreading diameter ($\xi(t)$) for different Weber numbers $We = 0.5, 10, 500$ with $\theta_s = 160^\circ$ and $Re = 800$.

surface tension and bounces off the solid surface. In this paper, we define such “jumping of the rim” as “splashing.” In reality, we expect that the surrounding gas will provoke instability of the jumping rim, which can break the cylindrical symmetry and form smaller droplets. Since our simulation is axisymmetric, we do not observe such symmetry breaking. However, we predict that in a full 3-d simulation, real splashing will occur in this case.

Fig. 7(b) shows that the outcome of the impact ranges from complete bouncing at $We = 0.5, 10$ to splashing at $We = 500$ on superhydrophobic surfaces ($\theta_s = 160^\circ$). Again, it is much easier to observe bouncing and splashing when the solid surface is more hydrophobic. The effect of wettability can be revealed by comparing Fig. 3(b) ($\theta_s = 110^\circ$ and $Re = 800$) and Fig. 7(b) ($\theta_s = 160^\circ$ and $Re = 800$). It is also seen from the impact map in Fig. 8(b) that superhydrophobicity allows bouncing to occur at a lower We . Physically, this is expected because the solid surface will repel a liquid droplet more energetically at a larger static contact angle, and consequently less kinetic energy is needed to induce bouncing.

D. Effect of slip length

In Fig. 10(a), we show the effect of slip length on the impact dynamics. As the slip length increases, both the advancing and receding processes accelerate and the maximum spreading diameter increases. The total contact time decreases with increasing slip length. Fig. 10(b) shows that the slip length does not have an appreciable effect on the outcome of the impact, at least not in the parameter region explored here.

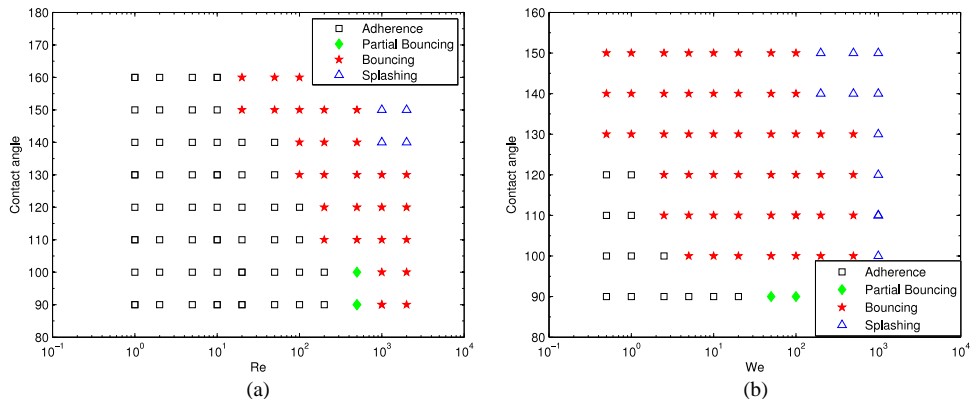


FIG. 8. (a) (Re, θ_s) impact map with a fixed $We = 150$. (b) (We, θ_s) impact map with a fixed $Re = 800$.

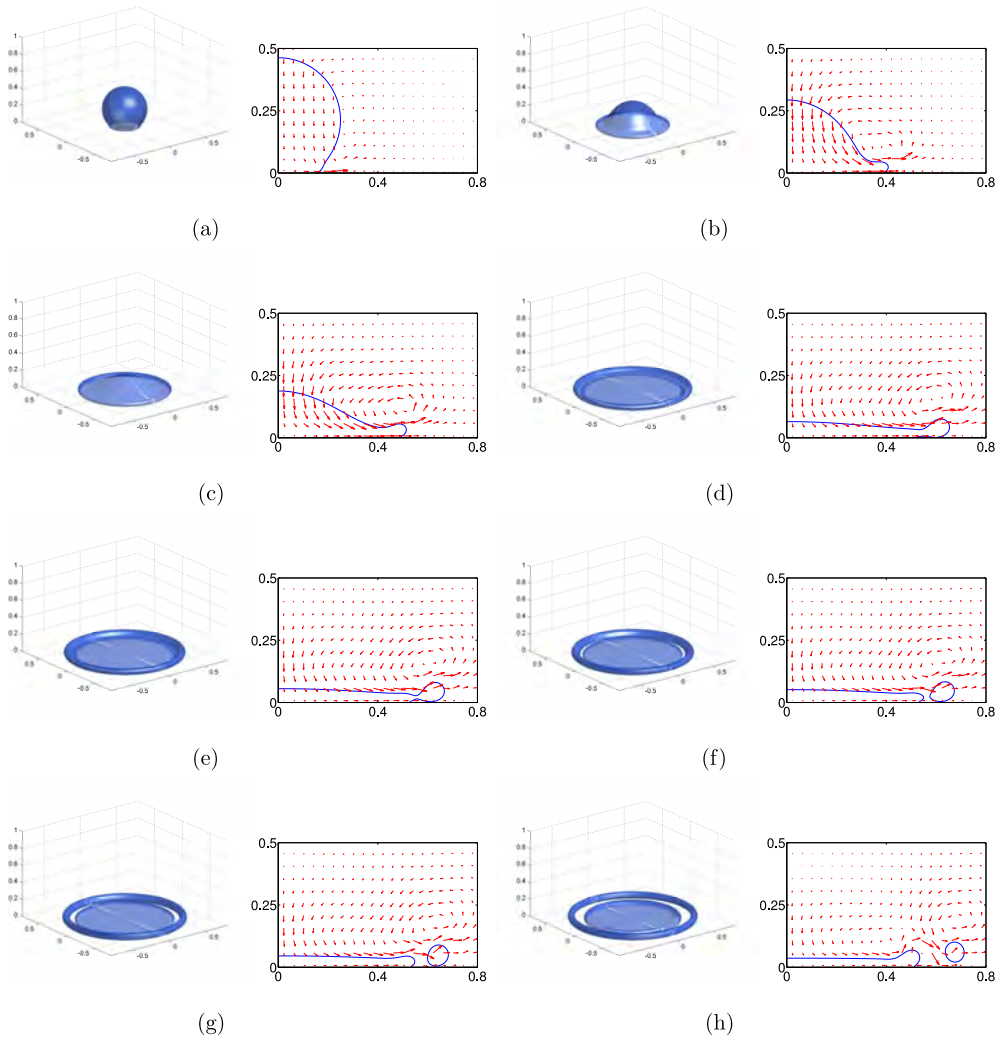


FIG. 9. Droplet shapes with the corresponding profiles (blue lines) and the corresponding velocity fields (red vectors) in the radial direction at different times obtained with $Re = 1000$ and $We = 150$, $\theta_s = 160^\circ$. (a) $t = 0.08$, (b) $t = 0.48$, (c) $t = 0.8$, (d) $t = 1.6$, (e) $t = 1.76$, (f) $t = 1.84$, (g) $t = 2.0$, and (h) $t = 2.4$.

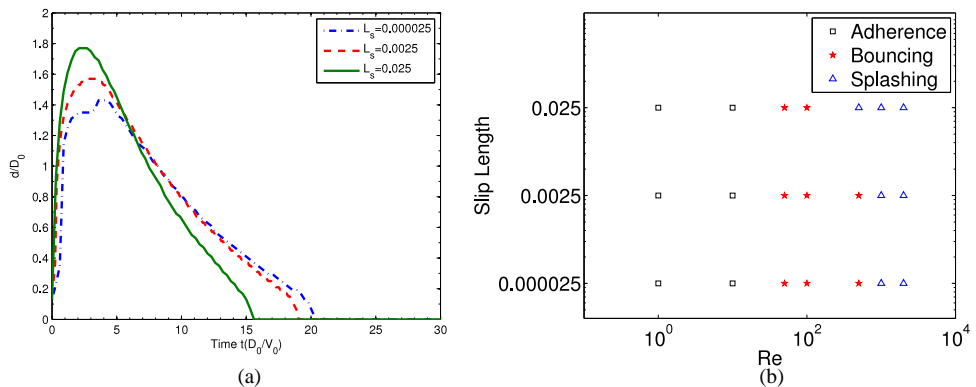


FIG. 10. (a) Time evolution of $\xi(t)$ for $\theta_s = 160^\circ$ with $We = 150$ and $Re = 50$. (b) (Re, \mathcal{L}_s) impact map at $\theta_s = 160^\circ$ and $We = 150$.

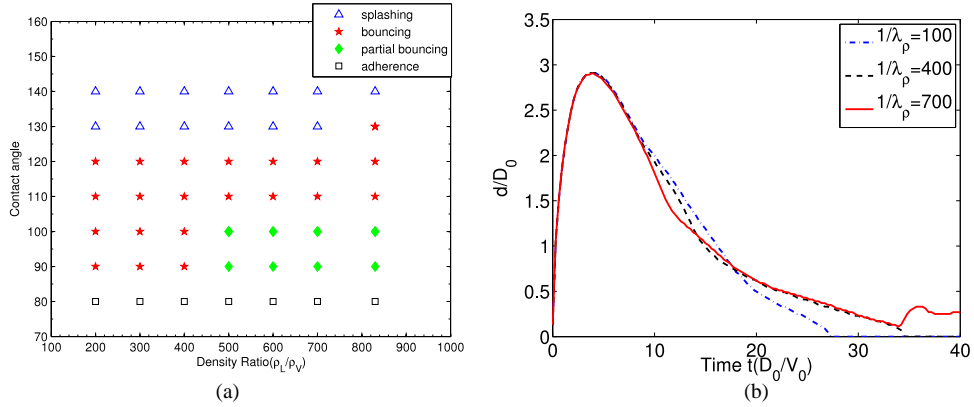


FIG. 11. (a) Impact map as a function of density ratio (ρ_L/ρ_V) and static contact angle (θ_s). (b) Time evolution of behavior of $\xi(t)$ with $\theta_s = 100^\circ$ for different density ratios.

Physically, the slip length measures the frictional coupling between the fluid and the solid surface. A larger slip length means a weaker coupling: the solid surface is less frictional. As a consequence, less free energy is dissipated in the spreading process upon droplet impact. This leads to a higher surface energy at the end of the spreading, and hence a larger maximum spreading diameter, as seen in Fig. 10(a). Furthermore, the recoil process is much slower than the spreading process. As a result, the dissipative forces, including the frictional force due to the boundary slip, become more important in the slow recoil than in the fast spreading. This is clearly seen in Fig. 10(a) where the slip length has a more visible effect on the recoil than on the spreading. A larger slip length means a less frictional solid surface, on which the recoil accelerates and the total contact time is shortened.

E. Effect of ambient fluid properties and equilibrium contact angle

In this section, we investigate how the density and viscosity of the ambient fluid affect the impact dynamics. The parameters in the numerical simulations are taken as

$$We = 200, \quad Re = 800, \quad \mathcal{L}_d = 1.0 \times 10^{-4},$$

$$\mathcal{V}_s = 500, \quad \mathcal{L}_s = 0.0025, \quad \lambda_{ls} = 1, \quad \epsilon = 0.01.$$

The different behaviors of a water droplet impacting on a smooth, non-wetting solid surface are summarized in the impact map shown in Fig. 11(a). The density ratio does not influence the impact dynamics much except near contact angle $\theta_s = 90^\circ - 100^\circ$, where the outcome of the impact changes from

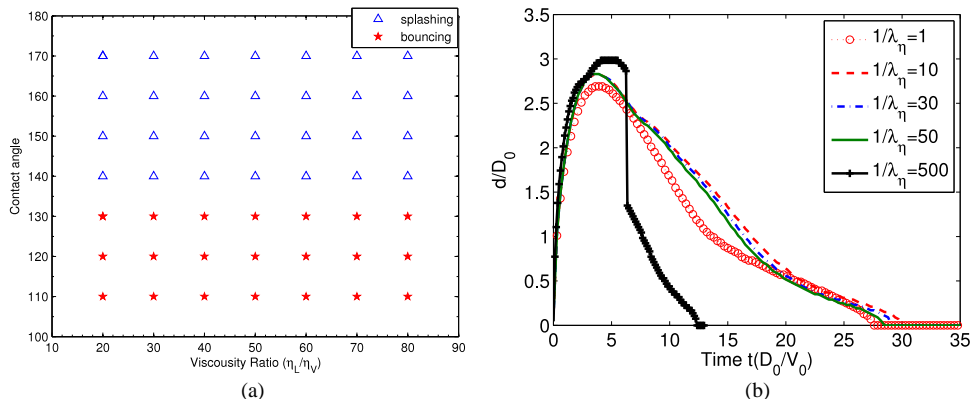


FIG. 12. (a) Impact map as a function of viscosity ratio (η_L/η_V) and static contact angle (θ_s). (b) Time evolution of behavior of $\xi(t)$ with $\theta_s = 110^\circ$ for different viscosity ratios.

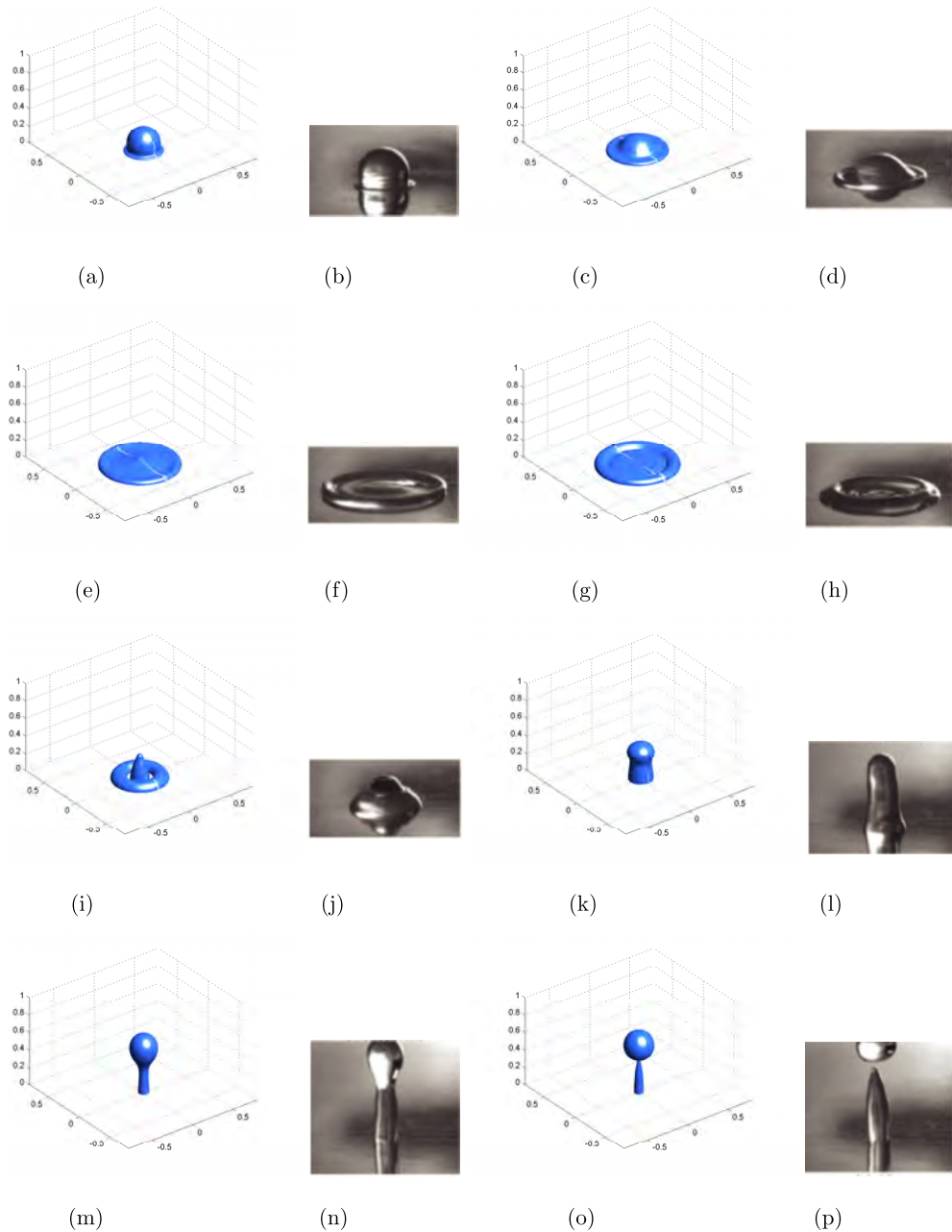


FIG. 13. Partial bouncing obtained for $Re = 3245$ and $We = 52$, $\theta_s = 100^\circ$. Simulation results and experiment results for dynamic process at time $t = 0.55$ ms (0.45 ms), 1.39 ms (1.31 ms), 3.07 ms (3.14 ms), 6.15 ms (6.02 ms), 10.90 ms (10.26 ms), 16.21 ms (14.02 ms), 25.16 ms (20.54 ms), and 27.96 ms (25.58 ms). Experiment figures courtesy of Rioboo *et al.*, “Time evolution of liquid drop impact onto solid, dry surfaces,” *Exp. Fluids* **33**, 112–124 (2002). Copyright 2002 Springer. (a) $t = 0.55$ ms, (b) $t = 0.45$ ms, (c) $t = 1.39$ ms, (d) $t = 1.31$ ms, (e) $t = 3.07$ ms, (f) $t = 3.14$ ms, (g) $t = 6.15$ ms, (h) $t = 6.02$ ms, (i) $t = 10.90$ ms, (j) $t = 10.26$ ms, (k) $t = 16.21$ ms, (l) $t = 14.02$ ms, (m) $t = 25.16$ ms, (n) $t = 20.54$ ms, (o) $t = 27.96$ ms, and (p) $t = 25.58$ ms.

bouncing to partial bouncing for large density ratios over $1/\lambda_\rho = 500$. This is because the observed phenomena are governed by a balance between the kinetic energy and total surface energy when We and Re are fixed. According to Eq. (23), $F_k/(F_{wf} + F_b)$ decreases as ρ_L/ρ_V increases. Fig. 11(b) shows $\xi(t)$ for three different density ratios. The advancing dynamics are not affected when the density ratio becomes large. The receding process, however, is quite different and we observe partial bouncing for larger density ratios.

The influence of the viscosity of the ambient fluid is investigated by varying the viscosity ratio $1/\lambda_\eta = \eta_L/\eta_V$ while keeping the density ratio constant, i.e., $1/\lambda_\rho = 830$. The different behaviors of a water droplet impacting on a smooth, non-wetting solid surface are summarized in the impact map shown in Fig. 12(a). Figs. 12(a) and 12(b) show that the change in viscosity ratio has only a slight effect on the dynamics of the impact when the viscosity ratio $1/\lambda_\eta \sim O(10)$. Further increasing the viscosity ratio from $O(10)$ to $O(100)$ (say $1/\lambda_\eta = 500$ in Fig. 12(b)), which implies a significant decrease in ambient fluid viscosity, leads to splashing phenomena. This is because \mathcal{R}_v and \mathcal{R}_s decrease as η_L/η_V increases.

F. Comparison with experimental results

Finally, we compare our numerical results to the experimental results. A case of partial bouncing in which a water droplet impacts on a wax surface with advancing contact angle $\theta_a = 110^\circ$ and receding contact angle $\theta_r = 90^\circ$ is taken from the experiments reported by Rioboo *et al.*²⁴ Since we only consider the static contact angle in our model, we simply take the static contact angle as the average of the advancing contact angle and the receding contact angle, i.e., $\theta_s = 100^\circ$. We use exactly the same parameters as in the experiment which, after scaling, are equivalent to $\rho_L/\rho_V = 830$, $\eta_L/\eta_V = 66.2$, $\mathcal{Re} = 3245$, and $\mathcal{We} = 52$ ($D_0 = 2.75$ mm and $V_0 = 1.18$ m/s see Table II in Rioboo *et al.*²⁴). Experimental results and numerical results are shown side by side in Fig. 13. We see almost quantitative agreement between the two sets of results in both the advancing and receding processes.

IV. CONCLUSION

We have used a phase field model to simulate the dynamics of a droplet impacting on a flat solid surface. We observe numerically droplet spreading, receding and rebounding (total and partial) off the solid surface. We study systematically the effect of the parameters (Reynolds number, Weber Number, density ratio, and viscosity ratio, and the equilibrium contact angle of the solid surface) on the dynamic process and outcome of the impact. The Reynolds number plays a dominant role in the spreading stage of the impact. But during droplet receding, the Weber number plays a more significant role. The wettability of the solid surface is found to affect the entire impact process. Bouncing and splashing are more likely to occur on hydrophobic surfaces. We also obtain near quantitative agreement with the experimental results, which demonstrates that our phase field model can satisfactorily describe the droplet impact phenomena.

ACKNOWLEDGMENTS

This publication was supported in part by the Hong Kong RGC-GRF Grant Nos. 605513 and 16302715 and the RGC-CRF Grant No. C6004-14G. We are also grateful to the anonymous referees for their valuable comments and suggestions.

APPENDIX: NUMERICAL IMPLEMENTATIONS

1. Time discretization

We use the numerical scheme proposed by Gao and Wang²⁰ to solve the CH and NS equations (11)-(19).^{6,7,14,23} The second order scheme can be summarized as

Step 1: Solve the CH equation using the convex-splitting method,

$$\left\{ \begin{array}{ll} \frac{3\phi^{n+1} - 4\phi^n + \phi^{n-1}}{2\delta t} + (\mathbf{v}^{n+1} \cdot \nabla)\phi^{*,n+1} = \mathcal{L}_d \nabla^2 \tilde{\mu}^{n+1}, & \text{in } (r, z) \in \Omega, \\ \frac{\phi^{n+1} - \phi^n}{\delta t} + v_r^{n+1} \partial_r \phi^{*,n+1} = -\mathcal{V}_s[\tilde{L}(\phi^{n+1})], \quad \partial_z \tilde{\mu}^{n+1} = 0, & \text{on } z = 0, \\ \partial_r \phi^{n+1} = 0, \quad \partial_r \tilde{\mu}^{n+1} = 0, & \text{on } r = 0, \\ \partial_r \phi^{n+1} = 0, \quad \partial_r \tilde{\mu}^{n+1} = 0, & \text{on } r = R/D_0, \\ \partial_z \phi^{n+1} = 0, \quad \partial_z \tilde{\mu}^{n+1} = 0, & \text{on } z = L/D_0, \end{array} \right. \quad (\text{A1})$$

where

$$\tilde{\mu}^{n+1} = -\epsilon \nabla^2 \phi^{n+1} + [s\phi^{n+1} - (1-s)\phi^{*,n+1} + (\phi^3)^{*,n+1}]/\epsilon, \tag{A2}$$

$$\tilde{L}(\phi^{n+1}) = \epsilon \partial_z \phi^{n+1} + \partial \gamma_{\omega f}(\phi^{*,n+1})/\partial \phi + \tilde{\alpha}(\phi^{n+1} - \phi^{*,n+1}). \tag{A3}$$

Step 2: Update ρ^n and η^n ,

$$(\rho^{n+1}, \eta^{n+1}, I_s^{n+1}) = \frac{1 - \phi^{n+1}}{2} + (\lambda_\rho, \lambda_\eta, \lambda_{I_s}) \frac{1 + \phi^{n+1}}{2}. \tag{A4}$$

Step 3: Solve the NS equation using the pressure stabilization scheme,

$$\begin{cases} \text{Re}[\rho^{n+1} \frac{3\mathbf{v}^{n+1} - 4\mathbf{v}^n + \mathbf{v}^{n-1}}{2\delta t} + \rho^{n+1}(\mathbf{v}^{*,n+1} \cdot \nabla)\mathbf{v}^{n+1}] \\ + \nabla(p^n + \frac{4}{3}\phi^n - \frac{1}{3}\phi^{n-1}) = \mathcal{B}\mu^{n+1}\nabla\phi^{n+1} + \nabla \cdot [\eta^{n+1}D(\mathbf{v}^{n+1})], & \text{in } (r, z) \in \Omega, \\ (\mathcal{L}_s I_s^{n+1})^{-1}(v_r^{slip})^{n+1} = \mathcal{B}L(\phi^{n+1})\partial_r \phi^{n+1}/\eta^{n+1} - \partial_z v_r^{n+1}, \quad v_z^{n+1} = 0, & \text{on } z = 0, \\ v_r^{n+1} = 0, \quad \partial_r v_z^{n+1} = 0, & \text{on } r = 0, \\ \partial_r v_r^{n+1} = 0, \quad \partial_r v_z^{n+1} = 0, & \text{on } r = R/D_0, \\ \partial_z v_r^{n+1} = 0, \quad v_z^{n+1} = 0, & \text{on } z = L/D_0, \end{cases} \tag{A5}$$

where

$$\mu^{n+1} = -\epsilon \Delta \phi^{n+1} - \phi^{n+1}/\epsilon + (\phi^{n+1})^3/\epsilon, \tag{A6}$$

$$L(\phi^{n+1}) = \epsilon \partial_n \phi^{n+1} + \partial \gamma_{\omega f}(\phi^{n+1})/\partial \phi. \tag{A7}$$

Step 4: Update pressure p according to

$$\begin{cases} \Delta \psi^{n+1} = \frac{3\bar{\rho}}{2\delta t} \text{Re} \nabla \cdot \mathbf{u}^{n+1}, & \text{in } (r, z) \in \Omega, \\ \partial_n \psi^{n+1} = 0, & \text{on } (r, z) \in \partial \Omega, \\ p^{n+1} = p^n + \psi^{n+1} - \eta^{n+1} \nabla \cdot \mathbf{u}^{n+1} & \text{on } (r, z) \in \Omega. \end{cases} \tag{A8}$$

Here, $(\cdot)^{*,n+1} = 2(\cdot)^n - (\cdot)^{n-1}$ and $\bar{\rho} = \min(1, \lambda_\rho)$.

To implement the above numerical schemes, we use the finite difference method to discretize space as mentioned in the next section and treat the nonlinear terms explicitly, i.e., $(\mathbf{v}^{n+1} \cdot \nabla)\phi^{*,n+1}$ as $(\mathbf{v}^n \cdot \nabla)\phi^{*,n+1}$, which will introduce a mild CFL-like constraint but will decouple the CH equation from the NS equation. Moreover, as the density ratio is large, we redistribute the phase variable ϕ like in Gao and Wang²⁰ to reduce the under-shots and over-shots near the interface.

2. Spatial discretization

The computational domain is

$$\Omega = \{(r, z) \mid 0 \leq r \leq \bar{R}, 0 \leq z \leq \bar{L}\}, \tag{A9}$$

where $r = 0$ corresponds to the z -axis (the centerline), $z = 0$ is the solid boundary where the droplet touches the surface and $\bar{R} = R/D_0$, $\bar{L} = L/D_0$. Divide Ω into $nz \times nr$ cells, with nz , nr being the number of cells in the z and r directions. The grid size is given by $\Delta z = \bar{L}/nz$ and $\Delta r = \bar{R}/nr$. The cell center, right boundary and top boundaries of the cell are represented by (i, j) , $(i + 1/2, j)$, and $(i, j + 1/2)$, respectively. The radial velocity v_r and axial velocity v_z are solved at the right and top boundaries of each cell, respectively, whereas the phase field ϕ , pressure p , and chemical potential μ are evaluated at the center of each cell (see Figure 14).

Second-order interpolations are used for variables evaluated at different grid points. For variables (denoted by u) solved on $(i + \frac{1}{2}, j)$,

$$u_{i,j} = \frac{u_{i-\frac{1}{2},j} + u_{i+\frac{1}{2},j}}{2}, \quad u_{i+\frac{1}{2},j+\frac{1}{2}} = \frac{u_{i+\frac{1}{2},j} + u_{i+\frac{1}{2},j+1}}{2}.$$

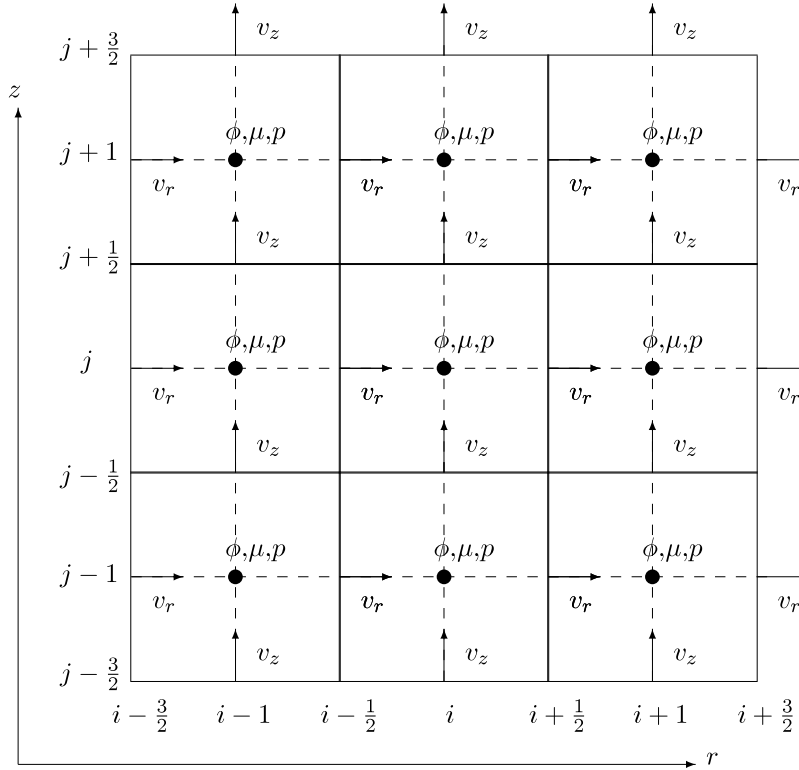


FIG. 14. Illustration of the staggered grid.

For variables (denoted by u) solved on $(i, j + \frac{1}{2})$,

$$u_{i,j} = \frac{u_{i,j-\frac{1}{2}} + u_{i,j+\frac{1}{2}}}{2}, \quad u_{i+\frac{1}{2},j+\frac{1}{2}} = \frac{u_{i,j+\frac{1}{2}} + u_{i+1,j+\frac{1}{2}}}{2}.$$

For variables (denoted by u) solved on (i, j) , the interpolation on the top boundary, right boundary and corner point are defined as follows:

$$u_{i+\frac{1}{2},j} = \frac{u_{i+1,j} + u_{i,j}}{2}, \quad u_{i,j+\frac{1}{2}} = \frac{u_{i,j+1} + u_{i,j}}{2},$$

$$u_{i+\frac{1}{2},j+\frac{1}{2}} = (u_{i+1,j+1} + u_{i+1,j} + u_{i,j+1} + u_{i,j})/4.$$

The differential operators are discretized as

$$\Delta u_{i,j} = \frac{u_{i,j+1} - 2u_{i,j} + u_{i,j-1}}{\Delta z^2} + \frac{r_{i+\frac{1}{2}}(u_{i+1,j} - u_{i,j}) - r_{i-\frac{1}{2}}(u_{i,j} - u_{i-1,j})}{r_i^2 \Delta r^2},$$

$$\Delta u_{i+\frac{1}{2},j} = \frac{u_{i+\frac{1}{2},j+1} - 2u_{i+\frac{1}{2},j} + u_{i+\frac{1}{2},j-1}}{\Delta z^2} + \frac{r_{i+1}(u_{i+\frac{3}{2},j} - u_{i+\frac{1}{2},j}) - r_i(u_{i+\frac{1}{2},j} - u_{i-\frac{1}{2},j})}{r_{i+\frac{1}{2}}^2 \Delta r^2},$$

$$\Delta u_{i,j+\frac{1}{2}} = \frac{u_{i,j+\frac{3}{2}} - 2u_{i,j+\frac{1}{2}} + u_{i,j-\frac{1}{2}}}{\Delta z^2} + \frac{r_{i+\frac{1}{2}}(u_{i+1,j+\frac{1}{2}} - u_{i,j+\frac{1}{2}}) - r_{i-\frac{1}{2}}(u_{i,j+\frac{1}{2}} - u_{i-1,j+\frac{1}{2}})}{r_i^2 \Delta r^2}.$$

An essential issue in the implementation is the treatment of the relaxation boundary condition. According to Eqs. (11) and (14), on the solid boundary, we have the consistency condition

$$\mathcal{L}_d \Delta \mu = -\mathcal{V}_s[L(\phi)], \quad \text{on } z = 0. \tag{A10}$$

This will replace Eq. (14) in the implementation. Therefore, if the grid points of μ and ϕ are $\mu_{i,j}$ and $\phi_{i,j}$, where $i = 0, \dots, nr - 1$ and $j = 0, \dots, nz - 1$, then on the solid boundary,

$$\mathcal{L}_d \Delta \mu_{i,-\frac{1}{2}}^{n+1} = -\mathcal{V}_s[L(\phi)]_{i,-\frac{1}{2}}^{n+1}, \tag{A11}$$

where the evaluation of $\Delta\mu$ on $(i, -1/2)$ is given as,

$$\begin{aligned}\Delta\mu_{i,-\frac{1}{2}} &= \frac{r_{i+\frac{1}{2}}(\mu_{i+1,-\frac{1}{2}} - \mu_{i,-\frac{1}{2}}) - r_{i-\frac{1}{2}}(\mu_{i,-\frac{1}{2}} - \mu_{i-1,-\frac{1}{2}})}{r_i\Delta r^2} - \frac{(\mu_{i,2} - 5\mu_{i,1} + 7\mu_{i,0} - 3\mu_{i,-1})}{8\Delta z^2} \\ &= \frac{r_{i+\frac{1}{2}}(\mu_{i+1,0} - \mu_{i,0}) - r_{i-\frac{1}{2}}(\mu_{i,0} - \mu_{i-1,0})}{r_i\Delta r^2} - \frac{(\mu_{i,2} - 5\mu_{i,1} + 4\mu_{i,0})}{8\Delta z^2}\end{aligned}$$

according to the boundary condition $\mu_{i,-1} = \mu_{i,0}$ and the second-order interpolation of μ on the boundary $z = 0$.

- ¹ A. Carlson, M. Do-Quang, and G. Amberg, "Modeling of dynamic wetting far from equilibrium," *Phys. Fluids* **21**, 121701 (2009).
- ² A. L. Yarin, "Drop impact dynamics: Splashing, spreading, receding, bouncing..." *Annu. Rev. Fluid Mech.* **38**, 152-192 (2006).
- ³ A. S. Moita and A. L. Moreira, "The deformation of single droplets impacting onto a flat surface," Society of Automotive Engineers 01-2749, 2002, pp. 1-13.
- ⁴ A. S. Moita and A. L. Moreira, "The dynamic behavior of single droplet impacting onto a flat surface," in ILASS-Europe, 2002.
- ⁵ D. Caviezel, C. Narayanan, and D. Lakehal, "Adherence and bouncing of liquid droplets impacting on dry surfaces," *Microfluid. Nanofluid.* **5**, 469-478 (2008).
- ⁶ D. J. Eyre, "Unconditionally gradient stable time marching the Cahn-Hilliard equation," in *Computational and Mathematical Models of Microstructural Evolution* (The Materials Research Society, Warrendale, PA, 1998), Vol. 529, pp. 39-46.
- ⁷ D. M. Anderson, G. B. McFadden, and A. A. Wheeler, "Diffuse-interface methods in fluid mechanics," *Annu. Rev. Fluid Mech.* **30**, 139-165 (1998).
- ⁸ D. Quéré, "Non-sticking drops," *Rep. Prog. Phys.* **68**, 2495-2532 (2005).
- ⁹ D. Richard and D. Quéré, "Bouncing water drops," *Europhys. Lett.* **50**, 769-775 (2000).
- ¹⁰ D. Richard, C. Clanet, and D. Quéré, "Surface phenomena: Contact time of a bouncing drop," *Nature* **417**, 811 (2002).
- ¹¹ G. N. Mercer, W. L. Sweatman, and W. A. Forster, "A model for crop spray adhesion bouncing and shatter at a leaf surface," in *Progress in Industrial Mathematics at ECMI* (Springer, 2008), Mathematics in Industry, Vol. 15, pp. 945-951.
- ¹² H. Xie, S. Koshizuka, and Y. Oka, "Numerical simulation of liquid drop deposition in annular-mist flow regime of boiling water reactor," *J. Nucl. Sci. Technol.* **41**, 569-578 (2004).
- ¹³ J. Fukai, Z. Zhao, D. Poulikakos, C. M. Megaridis, and O. Miyatake, "Modeling of the deformation of a liquid droplet impinging upon a flat surface," *Phys. Fluids A* **5**, 2588-2599 (1993).
- ¹⁴ J.-L. Guermond and A. Salgado, "A splitting method for incompressible flows with variable density based on a pressure Poisson equation," *J. Comput. Phys.* **228**, 2834-2846 (2009).
- ¹⁵ J. Zhu, L. Q. Chen, J. Shen, and V. Tikare, "Coarsening kinetics from a variable-mobility Cahn-Hilliard equation: Application of a semi-implicit Fourier spectral method," *Phys. Rev. E* **60**, 3564-3572 (1999).
- ¹⁶ K. Okumura, F. Chevy, D. Richard, D. Quéré, and C. Clanet, "Water spring: A model for bouncing drops," *Europhys. Lett.* **62**, 237-243 (2003).
- ¹⁷ K. Yokoi, D. Vadhillo, J. Hinch, and I. Hutchings, "Numerical studies of the influence of the dynamic contact angle on a droplet impacting on a dry surface," *Phys. Fluids* **21**, 072102-1-072102-12 (2009).
- ¹⁸ L. Xu, W. W. Zhang, and S. R. Nagel, "Drop splashing on a dry smooth surface," *Phys. Rev. Lett.* **94**, 184505-1-184505-4 (2005).
- ¹⁹ M. Gao and X.-P. Wang, "A gradient stable scheme for a phase field model for the moving contact line problem," *J. Comput. Phys.* **231**, 1372-1386 (2012).
- ²⁰ M. Gao and X.-P. Wang, "An efficient scheme for a phase field model for the moving contact line problem with variable density and viscosity," *J. Comput. Phys.* **272**, 704-718 (2014).
- ²¹ M. Nosonovsky and B. Bhushan, *Multiscale Dissipative Mechanisms and Hierarchical Surfaces* (Springer, 2008).
- ²² P. Attane, F. Girard, and V. Morin, "An energy balance approach of the dynamics of drop impact on a solid surface," *Phys. Fluids* **19**, 012101-1-012101-16 (2007).
- ²³ P.-H. Chiu and Y.-T. Lin, "A conservative phase field method for solving incompressible two-phase flows," *J. Comput. Phys.* **230**, 185-204 (2011).
- ²⁴ R. Rioboo, M. Marengo, and C. Tropea, "Time evolution of liquid drop impact onto solid, dry surfaces," *Exp. Fluids* **33**, 112-124 (2002).
- ²⁵ S. F. Lunkad, V. V. Buwa, and K. D. P. Nigam, "Numerical simulations of drop impact and spreading on horizontal and inclined surfaces," *Chem. Eng. Sci.* **62**, 7214-7224 (2007).
- ²⁶ S. Guo, M. Gao, X. Xiong, Y.-J. Wang, X.-P. Wang, P. Sheng, and P. Tong, "Direct measurement of friction of a fluctuating contact line," *Phys. Rev. Lett.* **111**, 026101 (2013).
- ²⁷ Š. Šikalo, M. Marengo, C. Tropea, and E. N. Ganić, "Analysis of impact of droplets on horizontal surfaces," *Exp. Therm. Fluid Sci.* **25**, 503-510 (2002).
- ²⁸ T. Lee and L. Liu, "Lattice Boltzmann simulations of micron-scale drop impact on dry surfaces," *J. Comput. Phys.* **229**, 8045-8063 (2010).
- ²⁹ T.-Z. Qian, X.-P. Wang, and P. Sheng, "Molecular scale contact line hydrodynamics of immiscible flows," *Phys. Rev. E* **68**, 016306 (2003).
- ³⁰ T.-Z. Qian, X.-P. Wang, and P. Sheng, "A variational approach to the moving contact line hydrodynamics," *J. Fluid Mech.* **564**, 333-360 (2006).

- ³¹ T.-Z. Qian, X.-P. Wang, and P. Sheng, "Molecular hydrodynamics of the moving contact line in two-phase immiscible flows," *Commun. Comput. Phys.* **1**, 1-52 (2006).
- ³² V. V. Khatavkar, P. D. Anderson, P. C. Duineveld, and H. E. Meijer, "Diffuse-interface modeling of droplet impact," *J. Fluid Mech.* **581**, 97-127 (2007).
- ³³ X.-P. Wang, T.-Z. Qian, and P. Sheng, "Moving contact line on chemically patterned surfaces," *J. Fluid Mech.* **605**, 59-78 (2008).
- ³⁴ Y. Renardy, S. Popinet, L. Duchemin, M. Renardy, S. Zaleski, C. Josserand, M. A. Drumright-Clarke, D. Richard, C. Clanet, and D. Quéré, "Pyramidal and toroidal water drops after impact on a solid surface," *J. Fluid Mech.* **484**, 69-83 (2003).
- ³⁵ Y. Tanaka, Y. Washio, M. Yoshino, and T. Hirata, "Numerical simulation of dynamic behavior of droplet on solid surface by the two-phase lattice Boltzmann method," *Comput. Fluids* **40**, 68-78 (2011).